Open Access Journal

Journal of Power Technologies 98 (2) (2018) 228–237

journal homepage:papers.itc.pw.edu.pl

Effect of anode porosity on the performance of molten carbonate fuel cell

Karol Ćwieka[a,*], Samih Haj Ibrahim[a], Jarosław Milewski[b], Tomasz Wejrzanowski[a]

[a] *Warsaw University of Technology, Faculty of Materials Science and Engineering, Woloska 141, 02-507 Warsaw, Poland*
[b] *Institute of Heat Engineering, Warsaw University of Technology, Nowowiejska 21/25, 00-665 Warsaw*

Abstract

Nickel anodes, for molten carbonate fuel cell (MCFC), of various porosities were fabricated using tape casting and firing processes. The same slurry composition but different sintering temperatures, 700 and 900℃, were used to obtain different anode porosities. Combined experimental and computational techniques were used to study the influence of anode porosity on the performance of molten carbonate fuels cell. The power generated by the 20.25 cm^2 class MCFC single cell was experimentally measured at 650℃ in humidified hydrogen with respect to the porosity of the anodes. The computational aspect involved the modeling of the microstructure of the sintered porous anodes which included measured size distribution of Ni powder used and porosities of the manufactured materials. For the best performing single cell, the optimal porosity for the nickel MCFC anode was experimentally determined to be 55%. Computations revealed that the specific surface area, which is a determining factor in electrochemical reactions, reaches a maximum at a porosity of 52%.

Keywords: anode, porosity, microstructure, performance, MCFC, modeling and simulation

1. Introduction

Molten carbonate fuel cells belong to a group of fuel cells that can be used as sources of highly stable electricity [1–3] and as chemical energy converters with a high fuel to energy conversion efficiency (over 60%) [4] and near or net zero emission of greenhouse gasses [5–9]. Currently, after successful commercialization of stationary units for distributed power generation, these types of fuel cells are being installed to supply hospitals and larger facilities where power stability is more important than operational cost. MCFC is still under development in terms of materials [10–15] and operational [13, 16–21] issues, however, its operating principles remain the same. The production of electric current is driven by electrochemical reactions and takes place over the electrode catalysts. Carbon dioxide and an oxidant (oxygen, air) react on the cathode to form carbonate ions:

$$^1/_2O_2 + CO_2 + 2e^- \longrightarrow CO_3^{2-} \quad (1)$$

which migrate through the electrolyte melt towards the anode to be finally consumed by oxidizing the fuel (hydrogen) and producing free electrons:

$$H_2 + CO_3^{2-} \longrightarrow H_2O + CO_2 + 2e^- \quad (2)$$

A molten carbonate fuel cell is both a solid oxide fuel cell (SOFC) and a high temperature fuel cell, since it operates at a temperature of 650℃. The elevated operational temperature of MCFCs is high enough to support an electrolyte (the mixture of carbonates) in a molten state, to produce sufficient ionic conductivity through the electrolyte and promote electrochemical electrode reactions (1) and (2). Generally, using lower operating temperatures reduces the degradation of fuel cell components, but on the other hand, a higher operating temperature enables MCFCs to operate with cheaper catalysts (than expensive platinum) for the anode reaction and increases resistance to fuel contaminants. Consequently, it facilitates the conversion (internal reforming) of hydrocarbon fuels, *i.e.* methane, methanol, crude oil and biofuels, into hydrogen [22–25]. This allows one to use a fuel different from pure hydrogen, which is not possible for low temperature ones *e.g.* a proton exchange membrane fuel cell (PEMFC).

The fuel cell efficiency and lifetime are limited by several factors, mainly related to chemical composition and microstructure of electrode materials [26, 27]. Nickel powder is still the most common base material for this application, due to its advantageous conjunction of features: chemical stability, catalytic performance at high temperature and competitive price, in comparison to other candidates *e.g.* noble metals like platinum [10, 11, 28].

Porosity, mean pore size and specific surface area are key

*Corresponding author
Email address: karol.cwieka.dokt@pw.edu.pl (Karol Ćwieka)

to arriving at a structure that promotes the fuel cell performance of an MCFC anode. Porosity, mean pore size and its distribution are of particular importance in terms of the sufficient transport of gaseous reactants, desorption and the removal of products into the pore space and the degree of infiltration by the electrolyte. Other characteristics of the pore space, such as: the tortuosity and constrictivity of the transport pathways, are significant for the optimization of the mass transport properties of open–porous materials [29–33]. An MCFC anode can be considered as an electrolyte reservoir with the degree of infiltration in the range of 50 .. 60% of its pore volume [34–36]. The active area for electrode reactions relates to the specific surface area which is a combination of porosity and mean pore size [37, 38]. The concept of a triple phase boundary (TPB), the region where catalyst, electrolyte and pore space (with gaseous reactants) combine, has been proposed to describe the electrode reactions in fuel cells [39–41]. Thus, the total length of the TPB within a material is an important factor to optimize for increasing the efficiency of both the electrode and the overall reactions [42–45]. According to the abovementioned requirements, the porosity of the MCFC anode typically ranges between 40 and 60% with a median pore diameter of about 5 µm, and a thickness of 0.7 .. 1.5 mm [11, 46]. These values have not, however, been justified as having been optimized by a physical understanding of their impact on the materials properties. Thus, more extensive studies are required for the design of the microstructure of anode material.

Computational methods combined with stochastic modeling are presently employed as a useful tool for the design of porous microstructures manufactured using different techniques [47–50]. In our previous study [51], we presented the approach for generating the structures of the porous MCFC cathode manufactured by a tape casting process. In the multi–step algorithm, the distribution of the mean particle size of nickel powder as well as the size and volume fraction of porogen, used as an additive which increases the porosity, were used to control the process. The amounts of the final ingredients correspond to those that were used during the slurry preparation stage of the tape casting process. The generated granular structures were further compared with micro–computed tomography (µ–CT) data of the manufactured materials in terms of the calculated structural parameters *i.e.* porosity, mean pore size and specific surface. Model data correlated with µ–CT data, so we employed similar methodology to design and quantify the structures of the manufactured MCFC anodes. A similar study, performed on solid oxide fuel cell (SOFC) anode in this case, was presented in [30].

In the present work, several green tapes with similar thickness were tape casted, sintered at 700 and 900 ℃ to obtain different porosities then characterized and tested under operating conditions. In the single–cell performance tests, values of cell voltage (E), power density (p) and current density (i) per unit area were measured for each of the manufactured anodes and the results are presented as E–i and p–i curves. The anode made by the Korean Institute of Science and Technology (KIST) was used as a reference meaterial. Experimentally measured power density was also usefully related to the microstructural features. To this end, the computational models of the microstructure of porous, tape casted MCFC electrodes based on a previously published approach, were employed.

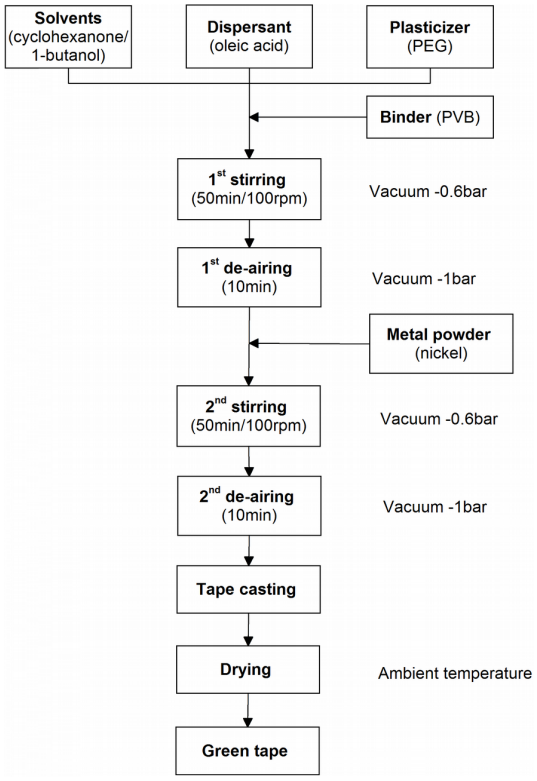

Figure 1: Flow chart of anode green tape fabrication process

2. Materials and methods

2.1. Anode preparation and characterization

The pure Ni anodes were fabricated according to the procedure schematically presented in Fig. 2.1. In the first stage, a mixture of solvents (cyclohexanone and 1 butanol, 1:1 wt. ratio), plasticizer (polyethylene glycol, PEG400) and dispersant (oleic acid) was prepared. After the addition of polyvinyl butyral (Mowital B60H, Kuraray) as a binder, a laboratory overhead stirrer was used to stir the mixture at 100 rpm for 1 h under vacuum conditions (0.6 bar). During the last 10 minutes of stirring the vacuum level was increased to 0.9 bar to eliminate any air bubbles from the mixture. In the second stage, pure Ni powder (purity 99.9%, average particle size ≈5 µm) was added as the solid content. The slurry was then stirred homogenously under the same time and vacuum conditions as in the preceding stage.

The as–prepared slurry was formed using the tape casting technique. Micrometer gauges on the doctor blade film

coater made it possible to set an initial thickness for forming the green tapes, herein set at 1.5 mm. Anode green tapes were obtained after drying at ambient temperature for 24 h. Green tapes were heat treated to remove the volatile contents at 200℃ for 2 h and polymeric binders at 400℃ for 2 h. Subsequently, the sintering stage was conducted under a reducing atmosphere of pure hydrogen at 700 and 900℃ for a holding time of 1 h.

The morphology of the nickel powder was identified using a Hitachi SU8000 scanning electron microscope (SEM) and the particle size distribution (PSD) was measured by using laser diffraction analysis (Kamika IPS U). The MCFC anode materials manufactured using the above procedure were also characterized using SEM. The samples for microstructural observations were cut out from the central part of manufactured anodes. Nickel powder and samples of nickel anodes were cleaned with acetone in ultrasonic bath to remove contaminants from the sufrace, and then dried at 50℃ for 1 h.

Porosity measurements were carried out based on the Archimedes' principle according to ASTM B962–13.

2.2. Experimental set-up

An experimental investigation was conducted to evaluate the performance of a single cell using anodes with various porosities. Each single–cell assembly was prepared by stacking the green sheets of electrolyte and matrix between sintered anode and cathode electrodes covered with current collectors. Then, the component assembly was held between cell frames equipped with channels made of 310 stainless steel (Fig. 2.2a) providing concurrent gas flow. The cell was tested in the experimental facility shown in Fig. 2.2b, where the cell was held in a vessel and it was possible to set up and control each operating parameter. The performance of the manufactured MCFC anodes was evaluated in a single–cell configuration with an effective electrode area of 20.25 cm^2. The anode had a porous nickel structure with a thickness of approx. 0.75 mm, the cathode had a porous (61%) *in situ* oxidized nickel structure with a thickness of 0.7 mm, the electrolyte a lithium and potassium carbonate $(Li_2CO_3)62/(K_2CO_3)38\%$ mixture. Three matrices of 0.3 mm thick each (0.9 mm in total) were applied.

Cell fabrication was completed on first heating ("cell conditioning"), during which the components took their final form due to the removal of the organic binder by thermal decomposition for 21 hours in air at temperatures ranging from 25 to 450℃ and then for 13 hours in H_2/CO_2 rich atmosphere at temperatures ranging from 450 to 650ºC. At about 500ºC the ceramic matrices and both the anode and the cathode electrodes were soaked with carbonate electrolyte. The temperature of the cell was monitored by two thermocouple probes in the center part of the cell frame and processed using a connected PC board. The thickness of the cell frames was about 2.5 cm to ensure isothermal conditions. An assembly pressure of 1.2 bar was applied to the single cell using an air cylinder for solid contact between components. All cells were of the co–flow type and operated under atmospheric conditions. The fuel gas $(H_2)80/(CO_2)20\%$ and the oxidant gas $(Air)70/(CO_2)30\%$ were fed in. The vaporizer system allowed one to both measure and control the water vapor directed at the anode and the cathode. Eight series of tests were performed at 650ºC, the temperature was kept constant at the cell plane using heating plates equipped with three electric heaters each. The cells were operated at atmospheric pressure with the same reference point, gas composition and flow rates. Dedicated software was used to preview and adjust the condition and performance of the system.

Cell voltage was directly measured at the two electrodes and its value was processed by a National Instruments board. Cell resistance was measured using HIOKI 3560 AC mΩ HiTESTER (four wires, 1 kHz). The gas composition and flow rates were controlled by a set of mass flow controllers. The gases and water flow rates were measured and controlled by Brooks 5850E Digital Mass Flow Controllers, chosen for their high accuracy and for their ability to be managed by software through serial PC ports. DC electronic load (SAE Electronic Conversion SRL) was used to supply the load.

2.3. Computational method

Stochastic numerical modeling was employed for the generation of representative models of open–porous structures manufactured by the tape casting of a slurry composed of metal particles suspended in polymeric binders. Furthermore, it was possible to generate structures with a porosity higher than what could be achieved by the manufacturing process. The granular model based on the μ–CT reconstructions of manufactured electrodes was implemented similar to our already published works [50–52]. The novelty of this methodology leads to new structure scenarios, rendering it possible to investigate geometrical features of the designed porous structures, since it incorporates particle size distribution of the same nickel powder, that was used in the manufacturing process of the MCFC anode. Validation against the results of the experimental characterization rendered computational models possible to resemble microstructures of tape cast anodes in their geometrical features. Powder particles in the model were represented by spheres.

In the first step, a set of polydisperse spheres was generated as representing the nickel powder particles. One thousand non–overlapping, spheres were randomly distributed in a cubic box (Fig. 2.3a). Then, a random close packing (RCP) algorithm [52] was used to iteratively pack these spheres in a bounding box with the smallest possible size, maintaining the condition of no overlap between them (Fig. 2.3b).

In the second step, the packed aggregate is processed using an iterative algorithm based on subsequent expansion and additive growth towards the formation of an open porous structure. The algorithm was coded using an APDL script (within ANSYS software). A single iteration begins with the selection of a number of spheres to be expanded. In the first iteration, these spheres, called seed points, are randomly selected from the packed aggregate. The number of seed

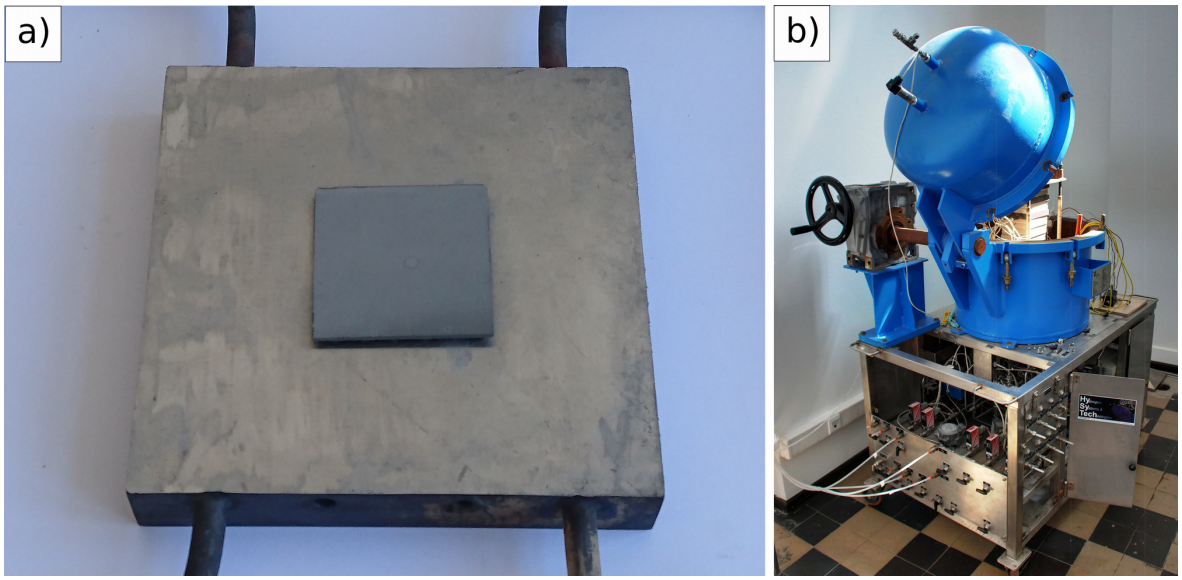

Figure 2: MCFC single-cell performance testing facilities: (a) the 20.25 cm^2cell frame, (b) testing rig.

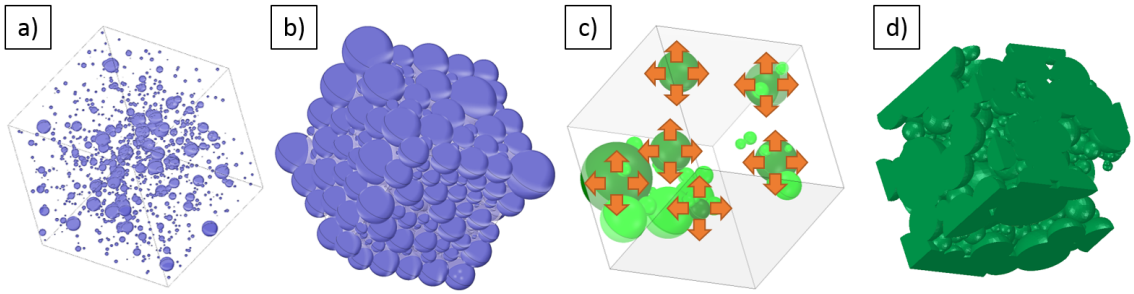

Figure 3: Schematic illustration of subsequent steps of MCFC anode structures generation: (a) set of polydisperse spheres; (b) spheres packing; (c) expansion of spheres and additive growth from initial points; d) resulting structure with desired porosity.

points have been optimized to achieve an adequate size of pores in the generated structure, since more seed points results in higher number of pores with a smaller average size. The expansion is performed by extending the radii of the spheres to find the intersections with the nearest neighbors (Fig. 2.3c). When an intersection between spheres occurs, they are added to the set of seed points assigned for the next iteration. The neighboring spheres that are in contact or intersect each other during the computational procedure, can not be deformed. The granular model used here has no capability to simulate interactions between the spheres representing nickel particles during the sintering process. After each iteration, the porosity is calculated as a difference between the volume of the bounding box and the volume of spheres. When the desired porosity is achieved, the iteration process is terminated, and the spheres are merged to form a solid skeleton that is finally clipped to the dimensions of cubic bounding box (Fig. 2.3d).

Image analysis was performed on the generated structures to provide information about their geometrical features. To this end, SkyScan CTan software was used. to calculate:

- final porosity as a difference between the volume of the bounding box and the volume of the spheres,
- mean pore size as a mean size of spheres inscribed into pore space,
- specific surface area as an area of internal pore surface divided by the volume of bounding box.

3. Results and discussion

3.1. Characterization of nickel powder

Nickel powder was characterized as the main constituent of the slurry and the base material of manufactured MCFC anodes.

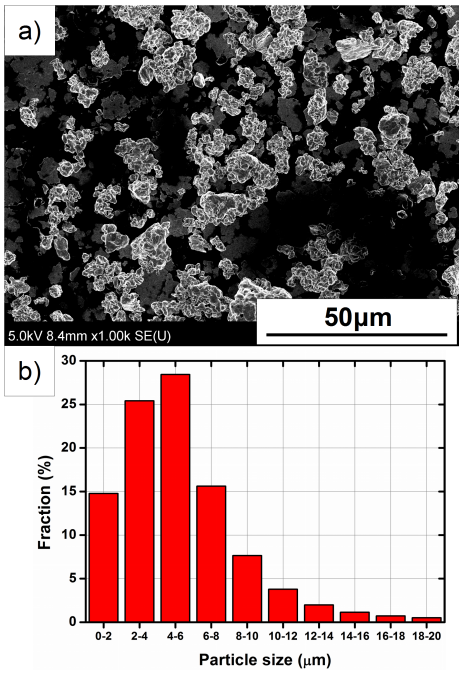

Figure 4: Scanning electron microscope image of the morphology of the nickel powder used in manufacturing process (a) and the particle size distribution (b).

SEM observations identified near equiaxial shaped nickel particles of predominantly rounded morphology with a narrow distribution of sizes (Fig. 4a). Particle size distribution measured using diffraction laser analysis showed d50 and d90 of 5.5 and 14 µm respectively. The distribution (Fig. 4b) was further used as input data for the numerical procedure for the generation of the anode structure models.

3.2. Characterization of sintered anodes

The microstructure of each MCFC anode was investigated in as sintered condition (see Fig. 5a,b). From each sintered green tape, 5×5 cm electrode tile was cut for performance tests. Unfortunately, the microstructures presented on SEM images may look similar and the difference in porosity may not be noticeable , particularly that these images present only the surface of the anode. SEM images cannot be used to quantify the porosity properly, but rather to made it possible to evaluate anode microstructure in terms of sintering quality and presence of residues of non–fired polymeric content (not observed in analyzed materials).

It has been already confirmed, that the thickness of the MCFC anode has a significant influence on the cell performance. Therefore, the thickness of the manufactured anodes were kept in the range of 0.73 .. 0.75 mm, similar to the KIST anode (reference). By contrast, the porosity was varied by using different sintering temperatures. It can be concluded that the anodes sintered at 900 ℃ have ≈30% lower porosity in comparison to those sintered in 700 ℃. Six anodes, indicated as A1–A6, were analyzed for further investigation. The thickness and porosity of these anodes are listed in Table 1 together with the sintering parameters used.

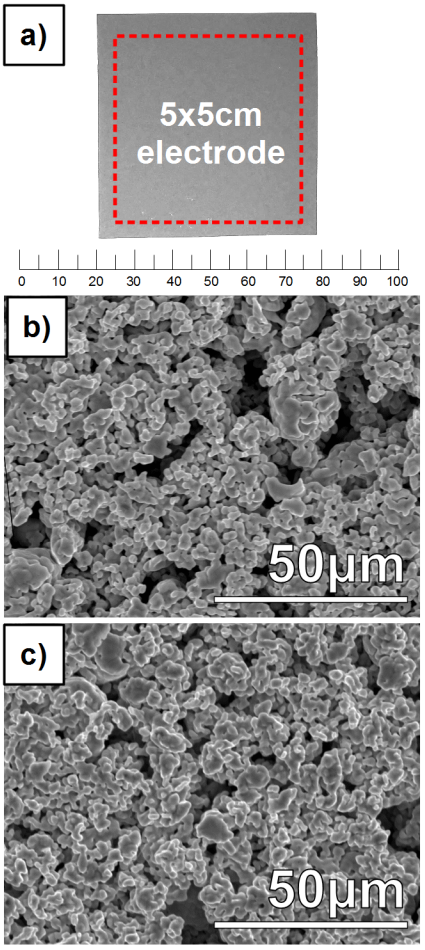

Figure 5: Anode in as-fired condition: (a) a macroscopic image with cutting lines for 5×5 cm electrode tile; SEM images of the microstructure of anodes sintered at: (b) 700 ℃ and (c) 900 ℃.

It is worth noting, that the anodes were manufactured with a porosity and thickness comparable to the KIST one, but using a sintering temperature of 700 ℃. Moreover, this temperature is much lower than 800 .. 900 ℃ which is reported in the literature for MCFC anode sintering.

3.3. Performance of the anodes in a single cell and the effect of porosity

The *E–i* and *p–i* curves resulting from the performance test of single cells assembled with manufactured anodes are shown in Fig. 9a and Fig. 9b, respectively. The experimental conditions were the same for each test, including other cell elements (cathode, matrix and electrolyte). The slopes in the Fig. 9a represent the electrical resistance of each single cell. Therefore, the difference in electrical resistance can be solely ascribed to the characteristics of the anode electrode used in the single cells.

In the present investigation, the performance of the anode layer was evaluated based on the maximum power density p_{max} generated in each cell. The results collected from in–cell performance tests revealed that the maximum power

Table 1: Sintering and structural parameters of manufactured anodes.

Anode	Sintering Temperature, ℃	Atmosphere	Thickness, mm	Porosity, % open	Porosity, % closed
KIST	800	100% H_2	0.74	55.0	n.d.
A1	900		0.75	37.8	4.7
A2			0.73	40.0	4.2
A3			0.74	41.4	4.1
A4	700		0.75	54.2	1.1
A5			0.74	55.6	0.8
A6			0.75	56.3	0.7

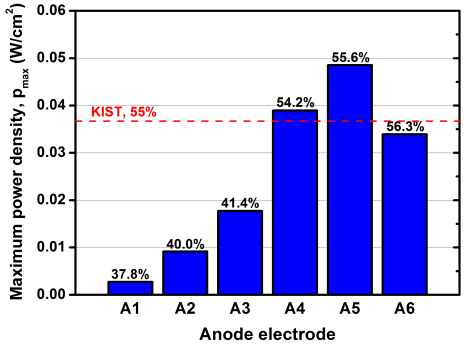

Figure 6: Experimental values of maximum power density generated by manufactured anodes.

density p_{max} =0.049 W/cm^2 was achieved by anode A5 with an open porosity of 55.6% (see Fig. 6).

For tape casted electrodes, porosity may be changed by the volume fraction of the polymeric binder in the slurry or by the temperature of sintering. Computational models enable us to predict that when the polymeric binder content is kept constant, an increase in sintering temperature results in the reduction of the open porosity, mainly due to the reduction of the mean pore size (Fig. 7a) and formation of closed pores (Table 1). The specific surface area, in turn, tends to increase together with the porosity only to some extent (Fig. 7b).

In the manufacturing route, open porosity of anodes was controlled applying different sintering temperatures, while the sintering time, the fraction of polymeric binder, and the nickel powder content were kept constant. Hence, the 'initial porous structure' (after polymer burnout) should be similar for each anode. Anodes sintered at 900℃ possessed lower open porosity than those sintered at 700℃, due to mass transport (diffusion) being increased with temperature. Higher sintering temperature strongly promotes an effect of closing small, initially open, pores what reduces both open porosity (P) and specific surface area (S_V). While open porosity regulates mass transport of gaseous reactants in the cell, closed porosity, in turn, has negative impact on this phenomenon since it reduces permeability of porous structure. In addition, the internal surface of closed pores becomes inaccessible for the gaseous reactants, so they cannot be delivered to active reaction sites on the electrode surface. The presence of closed porosity decreases the cell performance. The reduction of porosity and better sintering quality simultaneously resulted in apparently higher mechanical strength properties of the anodes sintered at 900℃.

Anodes sintered at 700℃ possessed porosities of 54.2, 55.6, and 56.3%. In this range of anode porosity, it was experimentally observed the optimum of molten carbonate fuel cell performance. Based on the analysis of the microstructure models, it can be explained that this optimum may be associated with the maximum of the specific surface area. Specific surface area (S_V), described as the internal surface area of pores in the unit volume, is crucial for the performance of the electrodes in a fuel cell, since it provides the effective area of a catalyst for chemical reactions to occur. The results of modeling predict a decrease in specific surface area when the porosity is larger than 52%. This theoretical optimum for catalytic reactions can be compared to the optimum measured porosity of 55% for fuel cell performance. Obtaining a higher porosity, above 55%, is possible when mean pore size becomes larger. However, mean pore size calculated based on models reveals only a slight difference between porosities of 52 and 59%, but significant decrease of S_V. Most probable is that the porosity above 55% may consist of a fraction of larger pores what means that the number of smaller ones is lower, and consequently the specific surface area decreases. It is possible that the higher porosity, the fraction of larger pores is more dominant, and the lower specific surface area.

Schematic explanation of the anode 'green microstructure' evolution during the sintering process at different temperatures is presented in Fig. 8. The differences in pore size between given microstructures were illustrated by inscribed spheres – a common method used in image analysis for pore size distribution measurements. Internal surface of pores divided by volue gives specific surface area (S_V).

The predominance of small pores in the microstructure of porous anodes, particularly with low open porosity, could be an additional disadvantage in terms of their performance. Small pores are responsible for capillary action—retention of the electrolyte from the matrix. As it has been reported in [53], the amount of electrolyte is consequently depleted and redistributed in the matrix, resulting in formation of voids. These voids are feasible channels for nitrogen crossover to occur. The higher concentration of nitrogen gas in the electrolyte may lead to decreasing the ionic conductivity between electrodes, and the cell performance.

Apart from differentiation of the sintering temperature, the microstructure of MCFC anodes may also be tailored with the use of pore forming particles, acting as space holders. The addition of such pore formers may render it possible

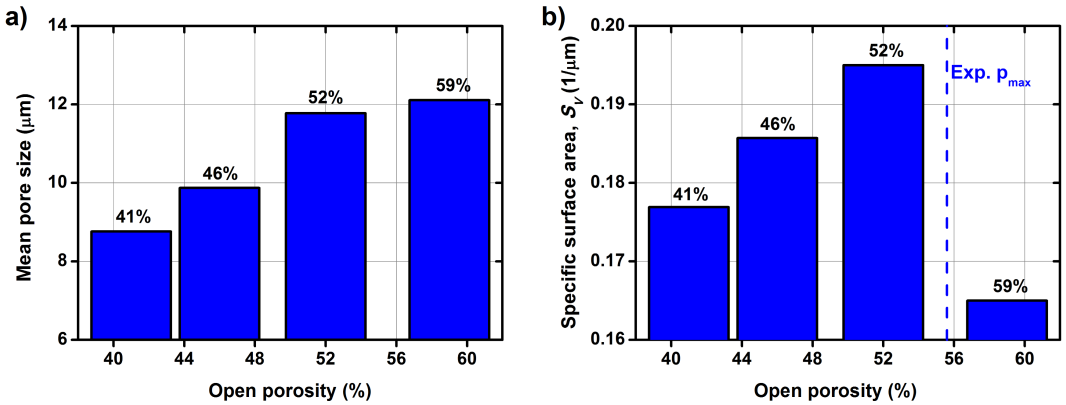

Figure 7: (a) mean pore size, and (b) specific surface area calculated as a function of porosity of numerical models. Porosity corresponding to maximum of p_{max} collected.

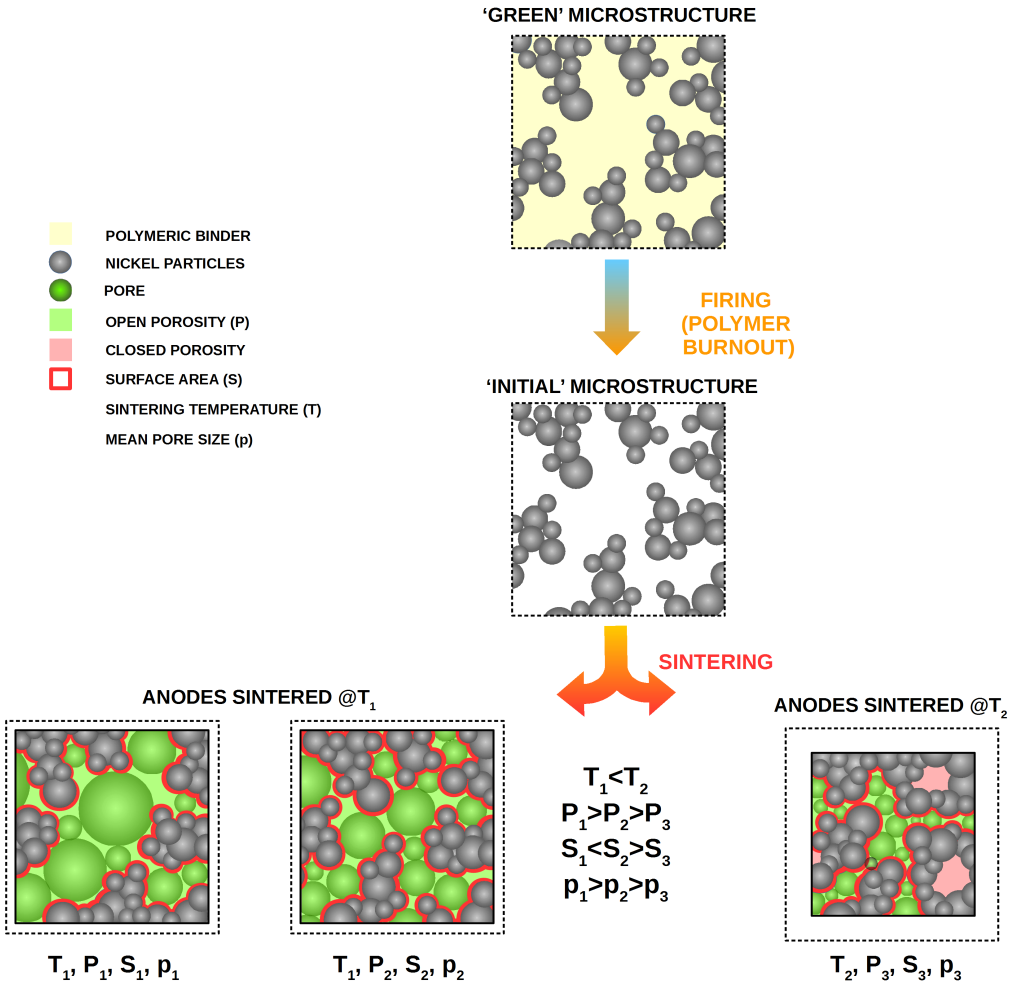

Figure 8: Schematic explanation of an anode 'green microstructure' evolution during the sintering process at different temperatures.

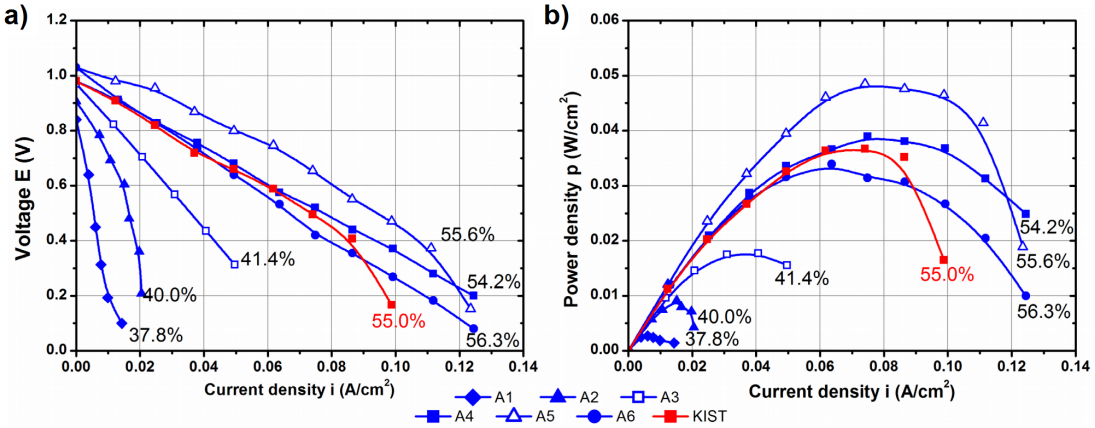

Figure 9: (a) *E–i*, (b) *p–i* curves collected from performance tests of single cells with manufactured anodes in comparison with the referential cell assembled of KIST materials with indication of anode open porosity.

to obtain different (open) porosity levels, pore size variation or pore shapes in materials sintered at the same temperature. The porosity may be substantially increased, compared to obtained without the use of pore formers. Pore size variation (isotropic or graded) introduced into elecrode microsturucture will affect its performance, since the fraction of pores of various size facilitates individual physico-chemical processes occuring *in operando*. To this end, particles of different size and shape may be added, for example starch and polyvinyl butyral (PVB) [27]. Therefore, the design of anode microstructure by addition pore formers combined with the performance study is very attractive for further research.

4. Conclusions

The effect of the porosity of anodes on the performance of MCFC has been studied. The highest power density obtained in this study for a MCFC was for a porosity of 55%. This may be explained by two competitive mechanisms influencing fuel cell performance at the anode side: the transport of the reagents and the catalytic reaction at the surface. Since the permeability of the gases is enhanced for higher porosity, the kinetics of the catalytic processes depend on the specific surface (through exchange current density). Computational modeling has been used to confirm that unfortunately porosity and specific surface area are intercorrelated. The model predicts the highest value for the S_V parameter of porosity of 52%. The optimum measured porosity, where the MCFC reaches the highest power density, is slightly higher (55%). This indicates that a compromise between the transport of gases and catalytic reactions is required.

Acknowledgements

This work has been financially supported by Polish National Centre for Research and Development under Contract No. PBS3/B4/14/2015.

References

[1] J. Brouwer, F. Jabbari, E. M. Leal, T. Orr, Analysis of a molten carbonate fuel cell: Numerical modeling and experimental validation, Journal of Power Sources 158 (1) (2006) 213–224. doi:10.1016/j.jpowsour.2005.07.093.

[2] H. Chen, T. N. Cong, W. Yang, C. Tan, Y. Li, Y. Ding, Progress in electrical energy storage system: A critical review, Progress in Natural Science 19 (3) (2009) 291–312. doi:10.1016/j.pnsc.2008.07.014.

[3] S. M. M. Ehteshami, S. H. Chan, The role of hydrogen and fuel cells to store renewable energy in the future energy network - potentials and challenges, Energy Policy 73 (2014) 103–109. doi:10.1016/j.enpol.2014.04.046.

[4] D. Cao, Y. Sun, G. Wang, Direct carbon fuel cell: Fundamentals and recent developments, Journal of Power Sources 167 (2) (2007) 250–257. doi:10.1016/j.jpowsour.2007.02.034.

[5] S. Campanari, P. Chiesa, G. Manzolini, CO_2 capture from combined cycles integrated with Molten Carbonate Fuel Cells, International Journal of Greenhouse Gas Control 4 (3) (2010) 441–451. doi:10.1016/j.ijggc.2009.11.007.

[6] S. Campanari, P. Chiesa, G. Manzolini, A. Giannotti, F. Federici, P. Bedont, F. Parodi, Application of MCFCs for active CO_2 capture within natural gas combined cycles, Energy Procedia 4 (2011) 1235–1242. doi:10.1016/j.egypro.2011.01.179.

[7] L. Caprile, B. Passalacqua, A. Torazza, Carbon capture: Energy wasting technologies or the MCFCs challenge?, International Journal of Hydrogen Energy 36 (16) (2011) 10269–10277. doi:10.1016/j.ijhydene.2010.10.028.

[8] S. Frangini, A. Masi, Molten carbonates for advanced and sustainable energy applications: Part I. Revisiting molten carbonate properties from a sustainable viewpoint, International Journal of Hydrogen Energy 41 (41) (2016) 18739–18746. doi:10.1016/j.ijhydene.2015.12.073.

[9] S. Frangini, A. Masi, Molten carbonates for advanced and sustainable energy applications: Part II. Review of recent literature, International Journal of Hydrogen Energy 41 (42) (2016) 18971–18994. doi:10.1016/j.ijhydene.2016.08.076.

[10] A. L. Dicks, Molten carbonate fuel cells, Current Opinion in Solid State and Materials Science 8 (2004) 379–383. doi:10.1016/j.cossms.2004.12.005.

[11] A. Kulkarni, S. Giddey, Materials issues and recent developments in molten carbonate fuel cells, Journal of Solid State Electrochemistry 16 (2012) 3123–3146. doi:10.1007/s10008-012-1771-y.

[12] J. Molenda, J. Kupecki, R. Baron, M. Blesznowski, G. Brus, T. Brylewski, M. Bucko, J. Chmielowiec, K. Cwieka, M. Gazda, A. Gil, P. Jasinski, Z. Jaworski, J. Karczewski, M. Kawalec, R. Kluczowski, M. Krauz, F. Krok, B. Lukasik, M. Malys, A. Mazur,

A. Mielewczyk-Gryn, J. Milewski, S. Molin, G. Mordarski, M. Mosialek, K. Motylinski, E. Naumovich, P. Nowak, G. Pasciak, P. Pianko-Oprych, D. Pomykalska, M. Rekas, A. Sciazko, K. Swierczek, J. Szmyd, S. Wachowski, T. Wejrzanowski, W. Wrobel, K. Zagorski, W. Zajac, A. Zurawska, Status report on high temperature fuel cells in Poland - recent advances and achievements, International Journal of Hydrogen Energy 42 (7) (2017) 4366–4403. doi:10.1016/j.ijhydene.2016.12.087.

[13] J. R. Selman, C. C. Chen, Scientific and technical maturity of molten carbonate technology, International Journal of Hydrogen Energy 37 (24) (2012) 19280–19288. doi:10.1016/j.ijhydene.2012.06.016.

[14] K. Czelej, K. Cwieka, K. J. Kurzydlowski, CO_2 stability on the Ni low-index surfaces: Van der Waals corrected DFT analysis, Catalysis Communications 80 (2016) 33–38. doi:10.1016/j.catcom.2016.03.017.

[15] K. Czelej, K. Cwieka, T. Wejrzanowski, P. Spiewak, K. J. Kurzydlowski, Decomposition of activated CO_2 species on Ni(110): Role of surface diffusion in the reaction mechanism, Catalysis Communications 74 (2016) 65–70. doi:10.1016/j.catcom.2015.10.034.

[16] C.-G. Lee, J.-Y. Hwang, S.-Y. Lee, M. Oh, D.-H. Kim, H.-C. Lim, Effect of anode area on the cell performance in a molten carbonate fuel cell, Journal of The Electrochemical Society 155 (2) (2008) 138–143. doi:10.1149/1.2815573.

[17] C.-W. Lee, M. Lee, M.-J. Lee, S.-C. Chang, S.-P. Yoon, H. C. Ham, J. Han, Effect of the flow directions on a 100cm^2 MCFC single cell with internal flow channels, International Journal of Hydrogen Energy (2016) 1–14doi:10.1016/j.ijhydene.2016.03.188.

[18] M. Cassir, S. J. McPhail, A. Moreno, Strategies and new developments in the field of molten carbonates and high-temperature fuel cells in the carbon cycle, International Journal of Hydrogen Energy 37 (24) (2012) 19345–19350. doi:10.1016/j.ijhydene.2011.11.006.

[19] D. Marra, Gas distribution inside an MCFC, International Journal of Hydrogen Energy 33 (12) (2008) 3173–3177. doi:10.1016/j.ijhydene.2008.03.005.

[20] S. M. C. Ang, E. S. Fraga, N. P. Brandon, N. J. Samsatli, D. J. Brett, Fuel cell systems optimisation - methods and strategies, International Journal of Hydrogen Energy 36 (22) (2011) 14678–14703. doi:10.1016/j.ijhydene.2011.08.053.

[21] S. H. Choi, D.-N. Nyeok Park, C. W. Yoon, S.-P. P. Yoon, S. W. Nam, S.-A. A. Hong, Y.-G. G. Shul, H. C. Ham, J. Han, A study on the electrochemical performance of 100-cm^2 class direct carbon-molten carbonate fuel cell (DC-MCFC), International Journal of Hydrogen Energy 40 (15) (2015) 5144–5149. doi:10.1016/j.ijhydene.2014.12.112.

[22] R. Bove, P. Lunghi, Experimental comparison of MCFC performance using three different biogas types and methane, Journal of Power Sources 145 (2) (2005) 588–593. doi:10.1016/j.jpowsour.2005.01.069.

[23] R. Ciccoli, V. Cigolotti, R. Lo Presti, E. Massi, S. J. McPhail, G. Monteleone, A. Moreno, V. Naticchioni, C. Paoletti, E. Simonetti, F. Zaza, Molten carbonate fuel cells fed with biogas: Combating H_2S, Waste Management 30 (6) (2010) 1018–1024. doi:10.1016/j.wasman.2010.02.022.

[24] V. Cigolotti, S. McPhail, A. Moreno, S. P. Yoon, J. H. Han, S. W. Nam, T. H. Lim, MCFC fed with biogas: Experimental investigation of sulphur poisoning using impedance spectroscopy, International Journal of Hydrogen Energy 36 (16) (2011) 10311–10318. doi:10.1016/j.ijhydene.2010.09.100.

[25] T. Watanabe, Y. Izaki, Y. Mugikura, H. Morita, M. Yoshikawa, M. Kawase, F. Yoshiba, K. Asano, Applicability of molten carbonate fuel cells to various fuels, Journal of Power Sources 160 (2) (2006) 868–871. doi:10.1016/j.jpowsour.2006.06.058.

[26] D. Seo, D. Park, S. Yoon, J. Han, I. Oh, Influence of the thin anode geometry on the performance of molten carbonate fuel cells, Transactions of the Korean Hydrogen and New Energy Society 22 (5) (2011) 599–608.

[27] T. Wejrzanowski, S. Haj Ibrahim, K. Cwieka, M. Loeffler, J. Milewski, E. Zschech, C.-G. Lee, Multi-modal porous microstructure for high temperature fuel cell application, Journal of Power Sources 373 (2018) 85–94. doi:10.1016/j.jpowsour.2017.11.009.

[28] X. Huang, G. Franchi, F. Cai, Characterization of porous bi-modal Ni structures, Journal of Porous Materials 16 (2) (2009) 165–173. doi:10.1007/s10934-007-9181-8.

[29] O. Stenzel, O. Pecho, L. Holzer, M. Neumann, V. Schmidt, Predicting effective conductivities based on geometric microstructure characteristics, AIChE Journal 62 (5) (2016) 1834–1843. doi:10.1002/aic.15160.

[30] G. Gaiselmann, M. Neumann, L. Holzer, T. Hocker, M. R. R. Prestat, V. Schmidt, Stochastic 3D modeling of $La_{0.6}Sr_{0.4}CoO_{3-\delta}$ cathodes based on structural segmentation of FIB-SEM images, Computational Materials Science 67 (2013) 48–62. doi:10.1016/j.commatsci.2012.08.030.

[31] G. Gaiselmann, M. Neumann, V. Schmidt, O. Pecho, T. Hocker, L. Holzer, Quantitative relationships between microstructure and effective transport properties based on virtual materials testing, AIChE Journal 60 (6) (2014) 1983–1999. doi:10.1002/aic.14416.

[32] M. Neumann, J. Staněk, O. M. Pecho, L. Holzer, V. Beneš, V. Schmidt, Stochastic 3D modeling of complex three-phase microstructures in SOFC-electrodes with completely connected phases, Computational Materials Science 118 (2016) 353–364. doi:10.1016/j.commatsci.2016.03.013.

[33] S. Haj Ibrahim, M. Neumann, F. Klingner, V. Schmidt, T. Wejrzanowski, Analysis of the 3D microstructure of tape-cast open-porous materials via a combination of experiments and modeling, Materials & Design 133 (2017) 216–223. doi:10.1016/j.matdes.2017.07.058.

[34] R. Bove, P. Lunghi, Experimental comparison of MCFC performance using three different biogas types and methane, Journal of Power Sources 145 (2) (2005) 588–593. doi:10.1016/j.jpowsour.2005.01.069.

[35] S.-G. Hong, J. R. Selman, Wetting characteristics of carbonate melts under MCFC operating conditions, Journal of The Electrochemical Society 151 (1) (2004) 77–84. doi:10.1149/1.1629094.

[36] J. Y. Youn, S. P. Yoon, J. Han, S. W. Nam, T. H. Lim, S. A. Hong, K. Y. Lee, Fabrication and characteristics of anode as an electrolyte reservoir for molten carbonate fuel cell, Journal of Power Sources 157 (1) (2006) 121–127. doi:10.1016/j.jpowsour.2005.07.068.

[37] M. Yoshikawa, A. Bodén, M. Sparr, G. Lindbergh, Experimental determination of effective surface area and conductivities in the porous anode of molten carbonate fuel cell, Journal of Power Sources 158 (1) (2006) 94–102. doi:10.1016/j.jpowsour.2005.09.038.

[38] R. Campbell, M. G. Bakker, C. Treiner, J. Chevalet, Electrodeposition of mesoporous nickel onto foamed metals using surfactant and polymer templates, Journal of Porous Materials 11 (2) (2004) 63–69. doi:10.1023/B:JOPO.0000027361.04282.f6.

[39] N. P. Brandon, D. J. Brett, Engineering porous materials for fuel cell applications, Philosophical transactions. Series A, Mathematical, physical, and engineering sciences 364 (1838) (2006) 147–159. doi:10.1098/rsta.2005.1684.

[40] K. Czelej, K. Cwieka, J. C. Colmenares, K. Kurzydłowski, Atomistic insight into the electrode reaction mechanism of cathode in Molten Carbonate Fuel Cell, J. Mater. Chem. A 5 (26) (2017) 13763–13768. doi:10.1039/c7ta02011b.

[41] K. Czelej, K. Cwieka, J. C. Colmenares, K. J. Kurzydlowski, Catalytic activity of NiO cathode in molten carbonate fuel cells, Applied Catalysis B: Environmental 222 (2018) 73–75. doi:10.1016/j.apcatb.2017.10.003.

[42] R. O'Hayre, D. M. Barnett, F. B. Prinz, The triple phase boundary. a mathematical model and experimental investigations for fuel cells, Journal of The Electrochemical Society 152 (2) (2005) A439–A444. doi:10.1149/1.1851054.

[43] S. Zhang, A. M. Gokhale, Computer simulations of topological connectivity of the triple phase boundaries in solid oxide fuel cell composite cathodes, Journal of Power Sources 219 (2012) 172–179. doi:10.1016/j.jpowsour.2012.07.049.

[44] V. M. Janardhanan, V. Heuveline, O. Deutschmann, Three-phase boundary length in solid-oxide fuel cells: A mathematical model, Journal of Power Sources 178 (1) (2008) 368–372. doi:10.1016/j.jpowsour.2007.11.083.

[45] T. Wejrzanowski, J. Gluch, S. H. Ibrahim, K. Cwieka, J. Milewski, E. Zschech, Characterization of spatial distribution of electrolyte in molten carbonate fuel cell cathodes, Advanced Engineering Materials (2018) 1700909.doi:10.1002/adem.201700909.

[46] J. R. Selman, Research, development, and demonstration of molten carbonate fuel cell systems, Springer US, Boston, MA, 1993, pp. 345–463.

[47] D. Stoyan, A. Wagner, H. Hermann, A. Elsner, Statistical characterization of the pore space of random systems of hard spheres, Journal of Non-Crystalline Solids 357 (6) (2011) 1508–1515.

doi:10.1016/j.jnoncrysol.2010.12.033.
[48] H. Hermann, A. Elsner, M. Hecker, D. Stoyan, Computer simulated dense-random packing models as approach to the structure of porous low-k dielectrics, Microelectronic Engineering 81 (2-4) (2005) 535–543. doi:10.1016/j.mee.2005.03.058.
[49] A. Bezrukov, M. Bargieł, D. Stoyan, Statistical analysis of simulated random packings of spheres, Particle and Particle Systems Characterization 19 (2) (2002) 111–118. doi:10.1002/ppsc.200600974.
[50] T. Wejrzanowski, S. H. Ibrahim, J. Skibinski, K. Cwieka, K. J. Kurzydlowski, Appropriate models for simulating open-porous materials, Image Analysis and Stereology 36 (2) (2017) 107–112. doi:10.5566/ias.1649.
[51] T. Wejrzanowski, S. H. Ibrahim, K. Cwieka, J. Milewski, K. J. Kurzydlowski, Design of open-porous materials for high-temperature fuel cells, Journal of Power Technologies 96 (3) (2016) 178–182.
[52] T. Wejrzanowski, J. Skibinski, J. Szumbarski, K. J. Kurzydlowski, Structure of foams modeled by Laguerre-Voronoi tessellations, Computational Materials Science 67 (2013) 216–221. doi:10.1016/j.commatsci.2012.08.046.
[53] H. Viet, P. Nguyen, M. Roslee, D. Seo, S. Pil, H. Chul, S. Woo, J. Han, J. Kim, Nano Ni layered anode for enhanced MCFC performance at reduced operating temperature, International Journal of Hydrogen Energy 39 (23) (2014) 12285–12290. doi:10.1016/j.ijhydene.2014.03.253.